Supplement of Biogeosciences, 18, 303–325, 2021
https://doi.org/10.5194/bg-18-303-2021-supplement

Biogeosciences
Open Access

Supplement of

A Lagrangian study of the contribution of the Canary coastal upwelling to the nitrogen budget of the open North Atlantic

Derara Hailegeorgis et al.

Correspondence to: Zouhair Lachkar (zouhair.lachkar@nyu.edu)

A Lagrangian study of the Canary coastal upwelling: Supplementary text and figures

Model evaluation

The model successfully simulates the Canary current flowing parallel to the Moroccan shore and its detachment from the coast and merger with the westward NEC around the latitude of Cape Blanc (Fig. S1). However, the strength of both the northward coastal Mauritanian current in the south (16-20°N) and the eastward Azores current in the north (34°N) is underestimated in the model in comparison to the drifter data. The model simulates successfully the surface Eddy kinetic energy (EKE, Fig. S1) in the central and most of the southern subregion as it reproduces quite accurately the high-EKE values observed downstream the Canary islands and the Cape Verde Archipelago and north of the Cape Verde Peninsula in Senegal (Fig. S1). However, the model tends to underestimate EKE associated with the Azores current in the northern part of the domain as well as south of the Cape Verde Peninsula. This might be due to the too weak Azores current in our model as well as the lack of high-frequency variability in the employed (climatological) forcing.

Despite a large-scale cold bias of around 1°C in the coastal region and throughout most of the northern part of the domain as well as a warm bias in the southern part of the domain, the model captures the main patterns of the observed sea-surface temperature (SST) from the Advanced Very High Resolution Radiometer (AVHRR) satellite data (Fig. S2). In particular, the model reproduces the observed offshore gradient in SST, as well as the offshore extent of the cold upwelling region. Additionally, the seasonal warming and cooling progression is relatively well depicted in the model (Fig S3). The model simulates the spatial pattern of the observed chlorophyll-a (Fig S2) reasonably well over much of the domain, with high-concentrations in the upwelling region and lower concentrations in the open oligotrophic ocean (Fig. S2). The north-south chlorophyll gradient is also well reproduced with the southern part of the Canary system being more productive than the northern part, in particular in winter and spring (Fig S4). However, the model underestimates the observed cholorophyll-a in the nearshore regions, particularly in the southern part of the domain (Fig S2 and Fig S4). Contrasting the modeled mixed layer depth (MLD) with observations indicates that much of the spatial and seasonal variability in upper ocean mixing is captured by the model (Fig S5). This is particularly true in the summer and fall when the simulated MLD agrees the most with observations.

In order to evaluate the model ability to reproduce the observed vertical patterns through seasons, we present comparisons of vertical cross sections of temperature, salinity and nitrate between the model and the World Ocean Atlas, for each of the three subregions and for the four seasons (from Fig S6 to Fig S14). This comparison suggests the model generally does a good job in reproducing the vertical variability in observations for all three variables across the different seasons. In particular, the depths of the thermocline, halocline and nutricline as well as their tilting near the coast are well captured by the model (from Fig S6 to Fig S14).

Finally, we contrast the POC profiles from the model to in situ observations by an ANT campaign (ANT 2005). This comparison shows that the model reproduces relatively well both the magnitude and the shape of the POC depth profiles in the CanCS (Fig S15).

A more quantitative evaluation of the model skill can be achieved using both satellite data and in situ observations from the World Ocean Database 2018 (WOD 2018). We binned the latter onto a 0.5° monthly climatology without any spatial interpolation. This permits us to compare the model and observations only in those grid points where observations are available. The results of this evaluation are summarized graphically using Taylor diagrams (Taylor, 2001) quantifying the similarity between the observations and model in terms of their correlation, the amplitude of their standard deviations and their centered root mean square difference (rmsd) (Fig. S3). We find that the simulated and observed mean SST have similar standard deviations and correlate very strongly with correlation coefficients above 0.95 for both nearshore and offshore regions (Fig. S3a). Similarly, the quantitative comparison of the simulated and observed sea surface salinity (SSS) shows similar standard deviations and a small rmsd, as well as very high correlations ($r > 0.9$) in the nearshore and throughout the domain. Mean surface nitrate in the model has a comparable variance but a weaker correlation ($r \approx 0.7$) with observations. Simulated mean surface chlorophyll-a is moderately ($0.6 < r < 0.8$) correlated with observations and displays a substantially weaker variance than the satellite data.

The seasonal anomaly of SST in the model agrees well with observations at all distances from the coast with both the correlation coefficient and normalized standard deviation being over 0.9 (Figure S3b). SSS seasonal anomalies in the model correlate less strongly with observations with both correlation coefficients and normalized standard deviations having values below 0.7. Simulated surface nitrate seasonal anomalies show very similar variance in comparison to observations but correlate only weakly with data ($0.3 < r < 0.5$). The simulated surface chlorophyll-a seasonal anomalies have a similarly weak correlation with the observations in addition to a lower normalized standard deviation (below 0.5).

We finally quantify the model ability to reproduce the three-dimensional distributions of temperature, salinity and nitrate in the upper ocean (Fig S17). At all depth ranges (top 100 m, top 400 m and top 1000 m), mean temperature, salinity and nitrate are all reproduced quite well with correlations above 0.9 and normalized standard deviations near 1. The seasonal anomalies (shown only for the depth range of 0 - 400 m), are less accurately captured by the model. Temperature anomaly in the top 400 m is captured relatively well with a correlation close to 0.8 and a standard deviation comparable to observations. Salinity and nitrate anomalies show lower correlations (0.3-0.4), diverge further in rmsd (close to 1) and have a narrower distribution with a standard deviation of around 0.6.

Comparison of offshore export of POC with previous studies

Several previous studies of the CanCS estimated the offshore transport of particulate organic carbon (POC) at various locations off the Northwest African coast (Table S4). For instance, Alonso-González et al. (2009) derived estimates of offshore transport of suspended POC in the upper ocean in a box model approach using in-situ measurements of POC and velocities based on geostrophy and Ekman contribution computed from non-locally sensed estimates. The POC export was quantified between 20°N and 29.2°N at two different transects at 20.6° W and 26° W for the top water column with a density of 26.44 kg m^{-3} or less. Their transport estimates exceed ours by around 45% and a factor five at 20.6° W and 26° W, respectively (Table S4). These discrepancies might result from the important sampling differences between the two studies, as our estimates correspond to annual-mean climatologies and are restricted to waters that upwell near the coast in contrast to the observational study. We also note that the mismatch between the two studies is particularly large for the deeper (0-135 m) and the further offshore (26° W) transect that is more likely to be affected by waters not directly related to coastal upwelling. García-Muñoz et al. (2004) and García-Muñoz et al. (2005) estimated the offshore transport of POC in the top 100 m associated with two filaments near C. Juby and C. Ghir, respectively. These estimates are nearly twice as large as ours (Table S4). Similarly, Santana-Falcon et al. (2016) inferred the offshore transport of POC associated with a filament near C. Ghir observed in August 2009 (Table S4). Their estimate exceeds our model-based annual-mean offshore transport estimate by almost a factor six (Table S4). Finally, we contrast annual mean POC offshore transport estimates by Lovecchio et al. (2017) to ours. While the transport figures by the two studies are relatively close between 17°N and 24.5°N at large offshore distances ($>$ 500 km), our estimated transport is nearly twice weaker in the nearshore and up to three times smaller at 1000 km between 24.5°N and 32°N (Table S4). While Lovecchio et al. (2017) is the only previous study that provides model-based large-scale annual mean estimates of the offshore transport of POC in the CanCS, it is based on Eulerian approach that does not distinguish between waters that originate from the coastal upwelling and the non-upwelling waters.

In summary, all previous studies reported here find higher estimates of POC offshore export in several portions of the CanCS. Our lower offshore transport estimates may at least partially result from our Lagrangian approach that focuses on coastally upwelled water only, disregarding non-upwelling waters and open ocean upwelling. Furthermore, restricting the analysis to upwelling particles in our study limits offshore flux to near-surface waters as most upwelled waters remain at very shallow depth. Finally, the loss of organic nitrogen due to sinking of particulate matter experienced by upwelling waters as they are exported offshore likely contributes to our overall lower transport estimates.

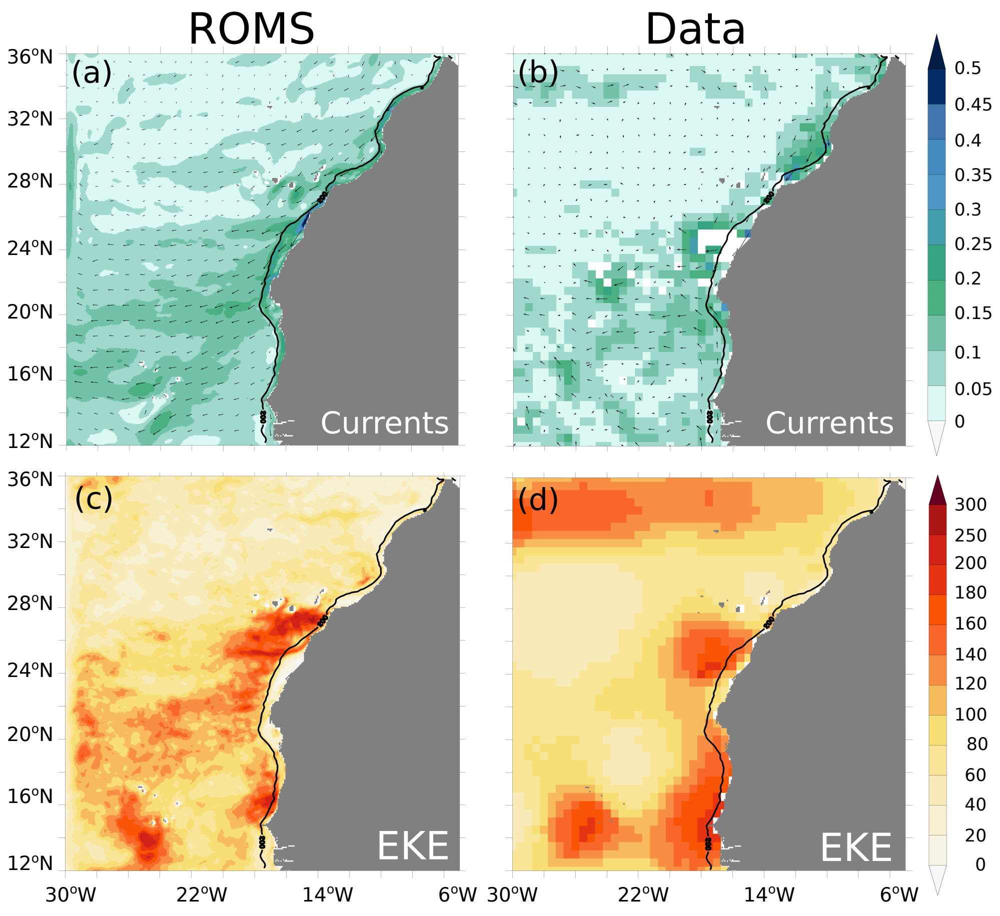

Figure S1. Surface (a-b) currents (in $\mathrm{m\,s^{-1}}$) and (c-d) eddy kinetic energy (in $\mathrm{cm^2\ s^{-2}}$) as simulated in the model (left) and from surface drifter climatology of Lumpkin and Johnson (2013) (right). (a-b) Arrows indicate the direction of the current and the color shading shows the current magnitude. The black line traces the shelf break at the 200 m isobath.

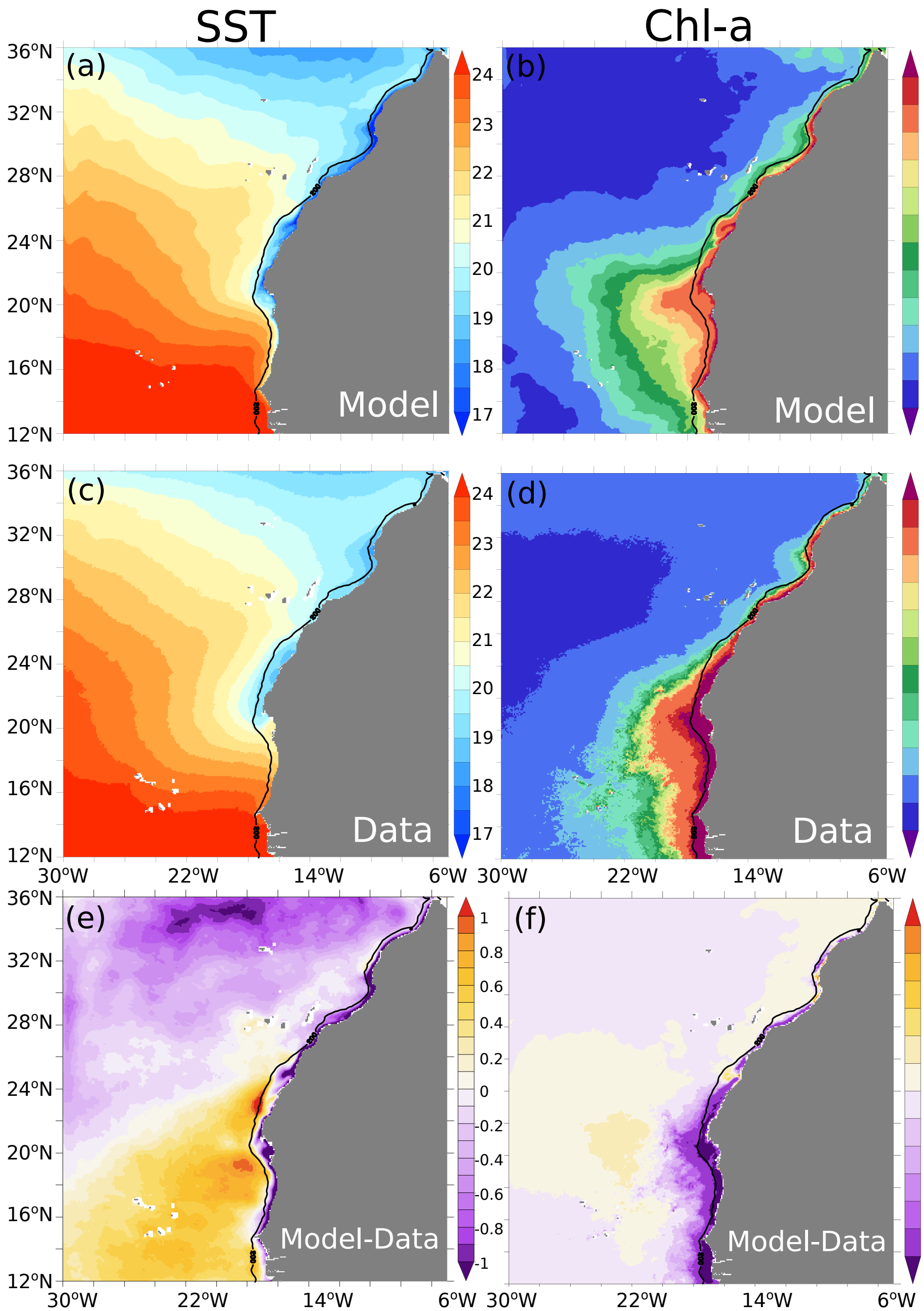

Figure S2. A comparison of sea surface temperature (in °C) and surface chlorophyll-a concentration (in mg m^{-3}) between the model and observations. We compare SST simulated in ROMS (a) with AVHRR data (c) and show their difference (e). We compare chlorophyll-a simulated in ROMS (b) with SeaWiFS data (d) and show their difference (f). The AVHRR and the SeaWiFS climatologies are computed over the periods from 1981 to 2016 and from 1997 to 2009, respectively. The black line traces the shelf break at the 200 m isobath.

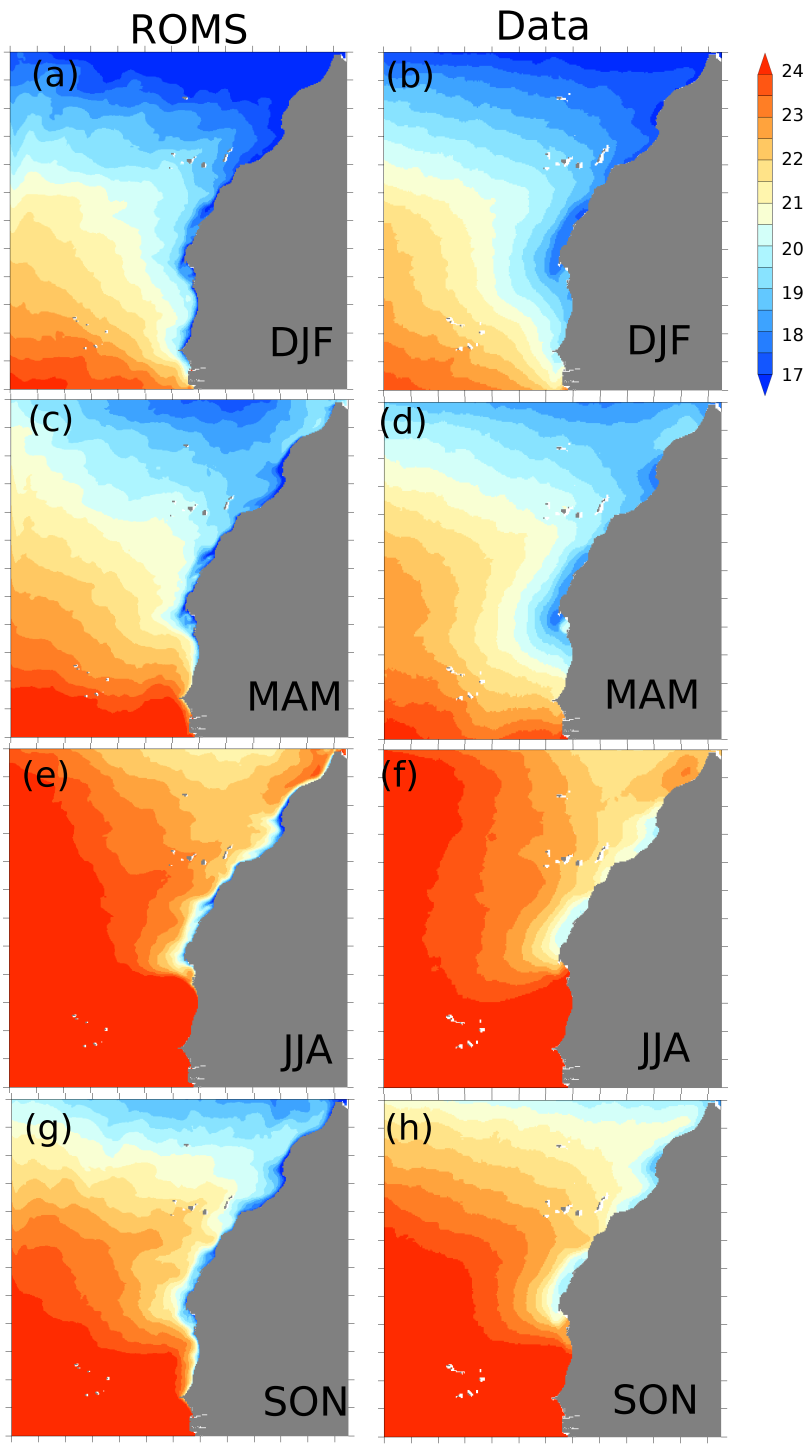

Figure S3. Sea surface temperature (in °C) as simulated in ROMS (left) and from AVHRR data (right) for all four seasons. The AVHRR seasonal climatologies are computed over the period from 1981 to 2016.

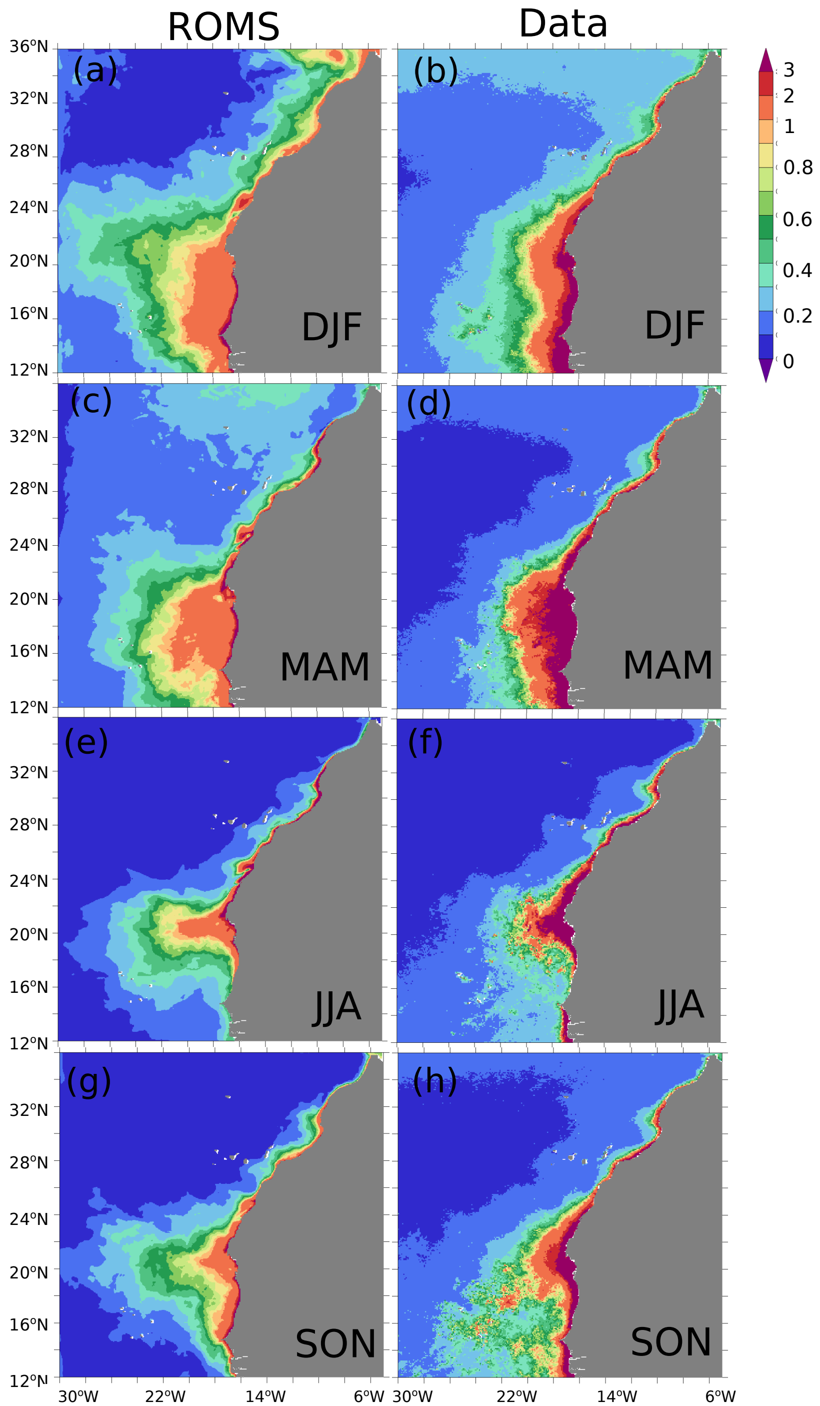

Figure S4. Chlorophyll-a concentrations (in $\mathrm{mg\,m^{-3}}$) as simulated in ROMS (left) and from SeaWiFS data (right) for all four seasons. The SeaWiFS seasonal climatologies are computed over the period from 1997 to 2009.

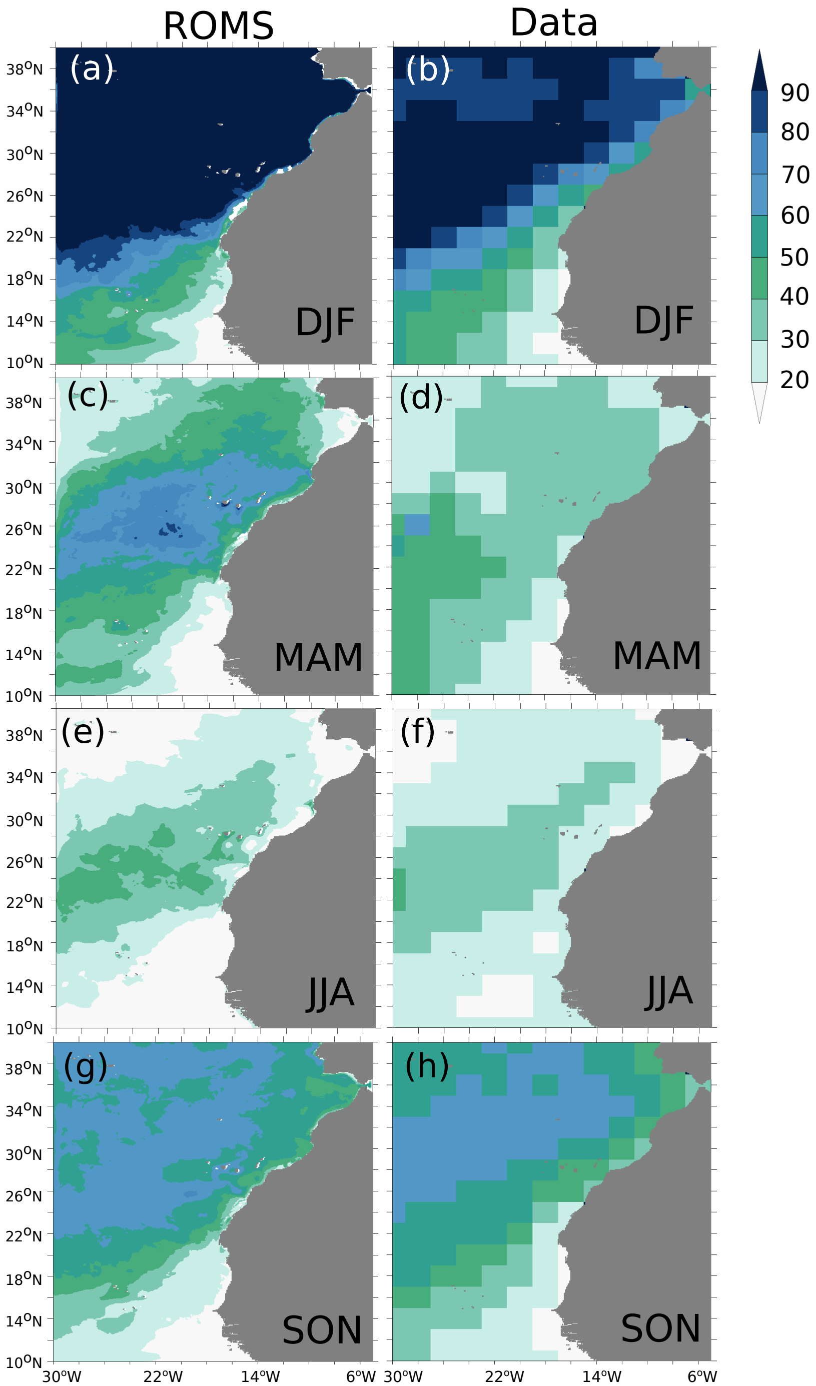

Figure S5. Comparison of mixed layer depth maps between the model and observations.

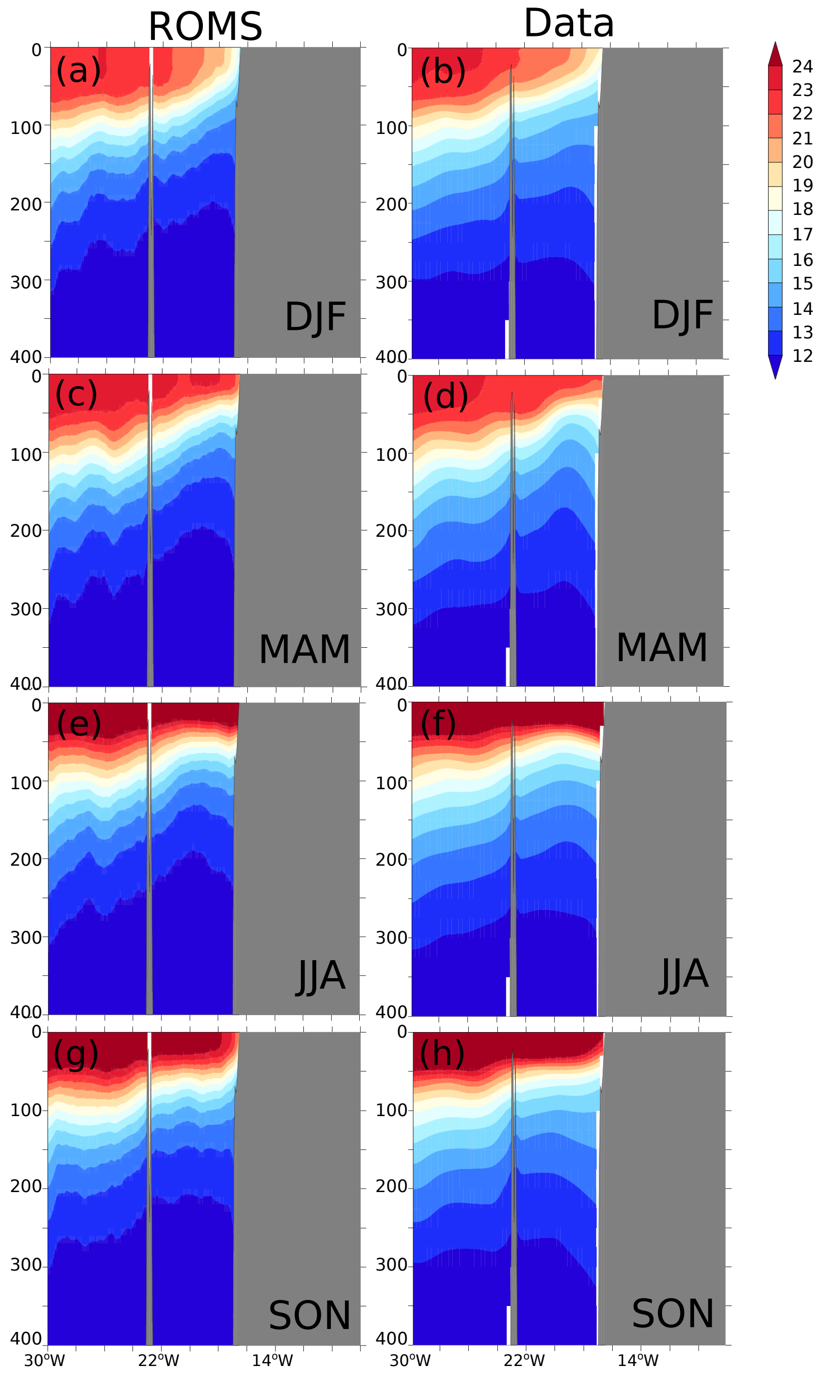

Figure S6. Comparison of vertical cross section of temperature across a transect at 16°N in the top 400m between the model and World Ocean Atlas observations.

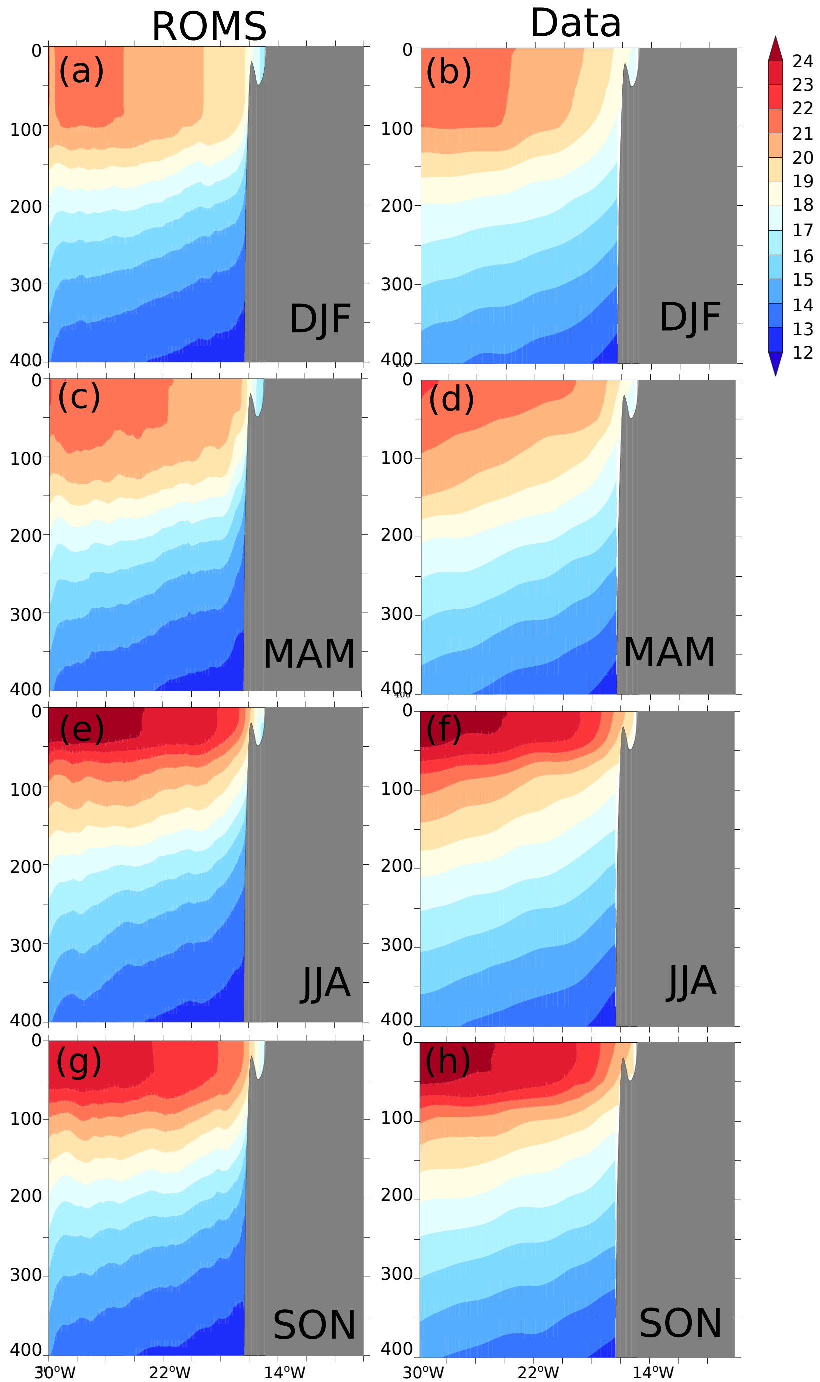

Figure S7. Comparison of vertical cross section of temperature across a transect at 25°N in the top 400m between the model and World Ocean Atlas observations.

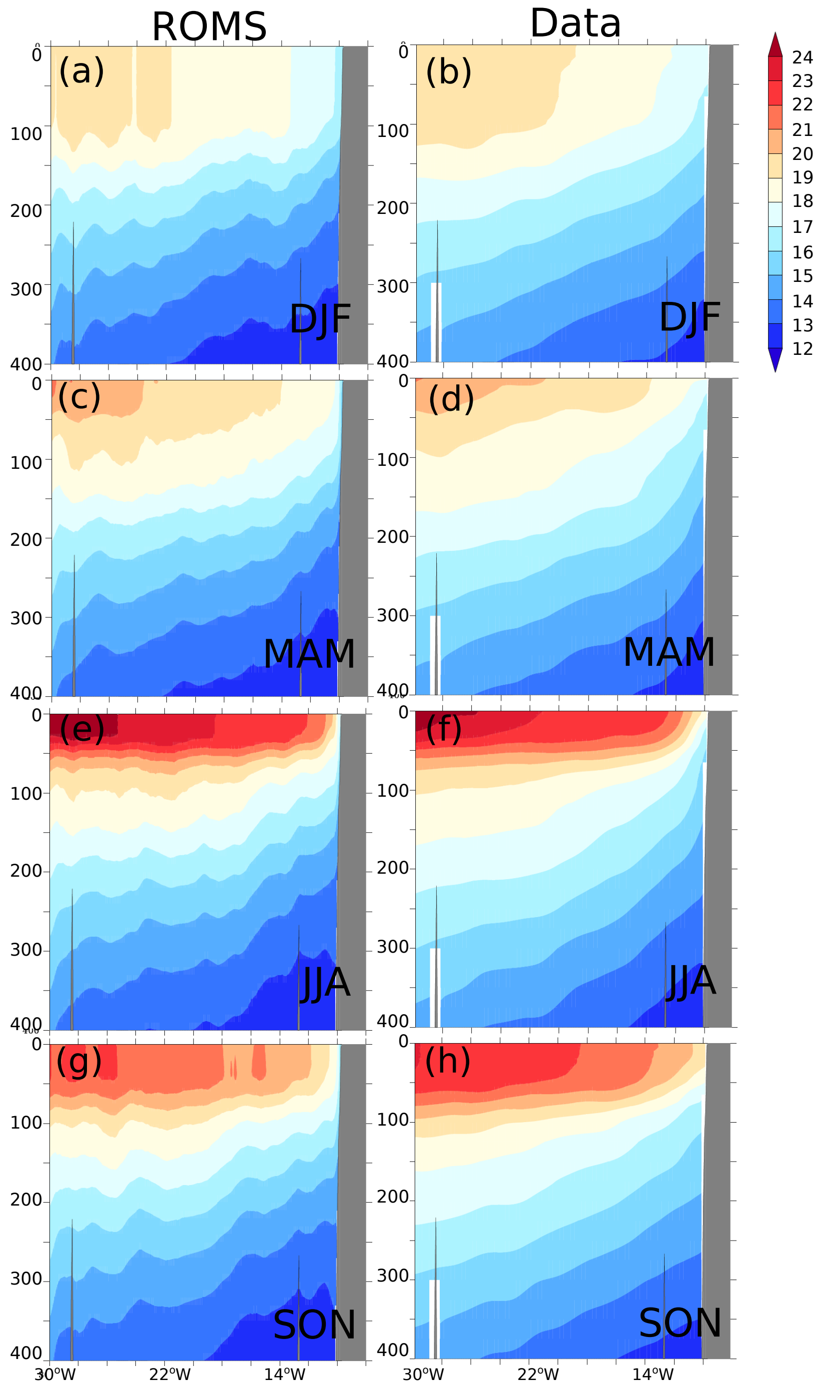

Figure S8. Comparison of vertical cross section of temperature across a transect at 30°N in the top 400m between the model and World Ocean Atlas observations.

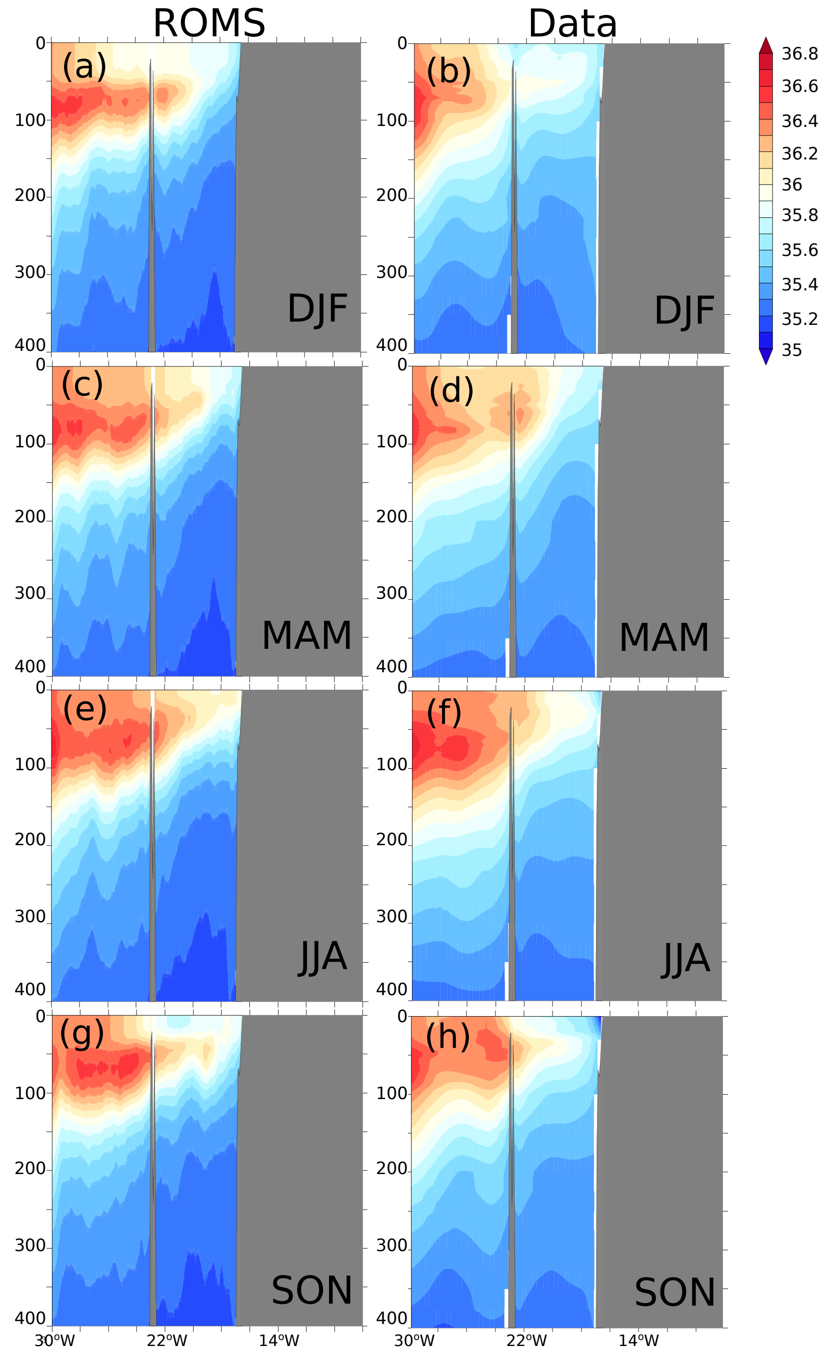

Figure S9. Comparison of vertical cross section of salinity across a transect at 16°N in the top 400m between the model and World Ocean Atlas observations.

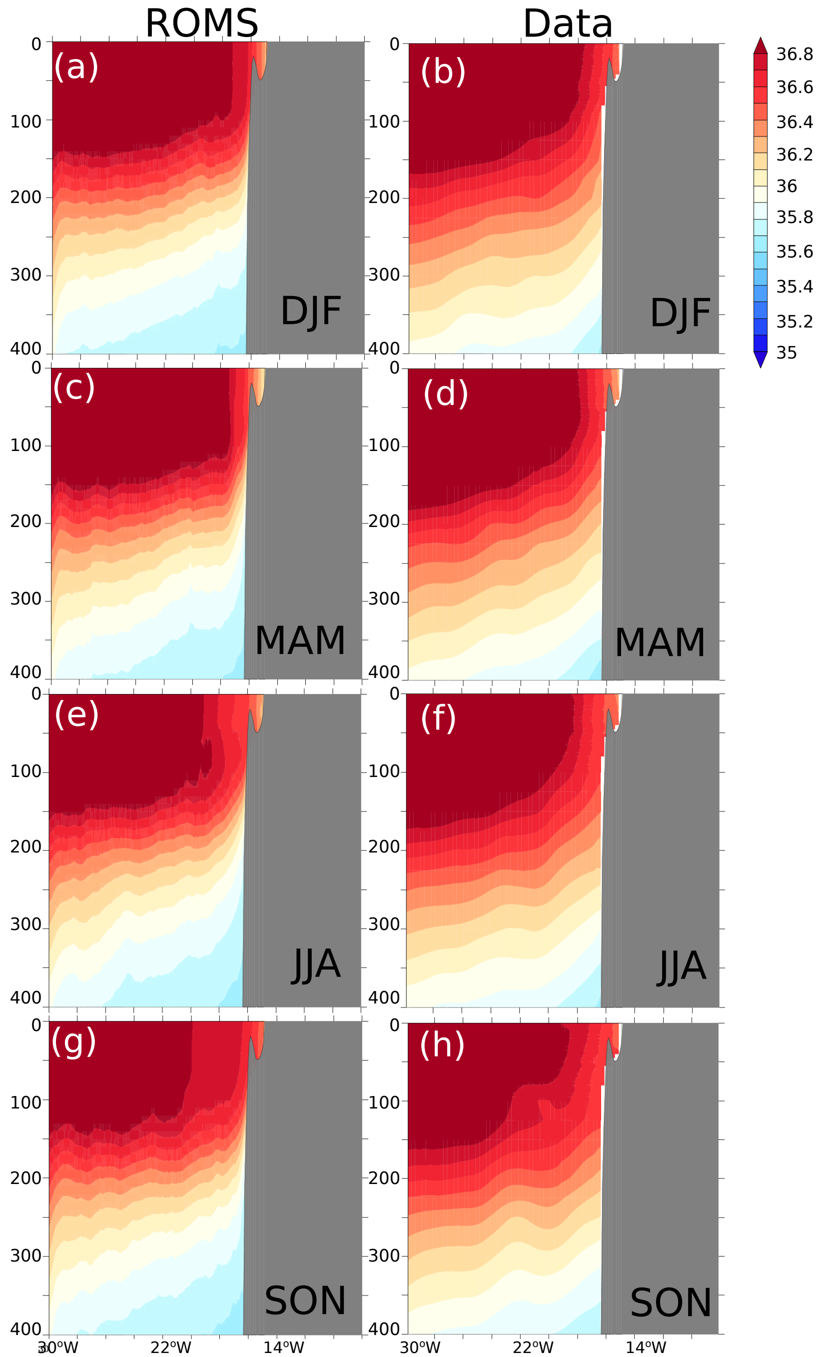

Figure S10. Comparison of vertical cross section of salinity across a transect at 25°N in the top 400m between the model and World Ocean Atlas observations.

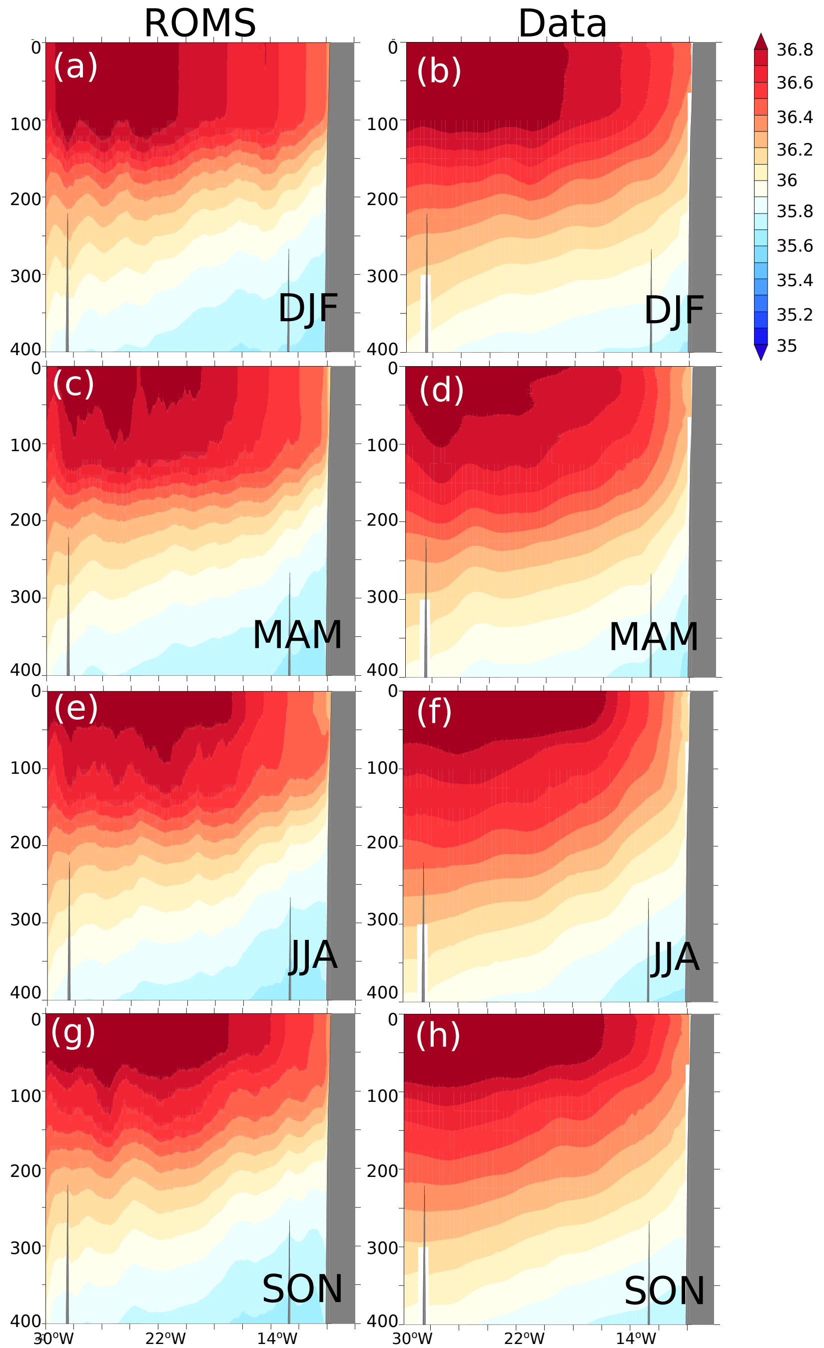

Figure S11. Comparison of vertical cross section of salinity across a transect at 30°N in the top 400m between the model and World Ocean Atlas observations.

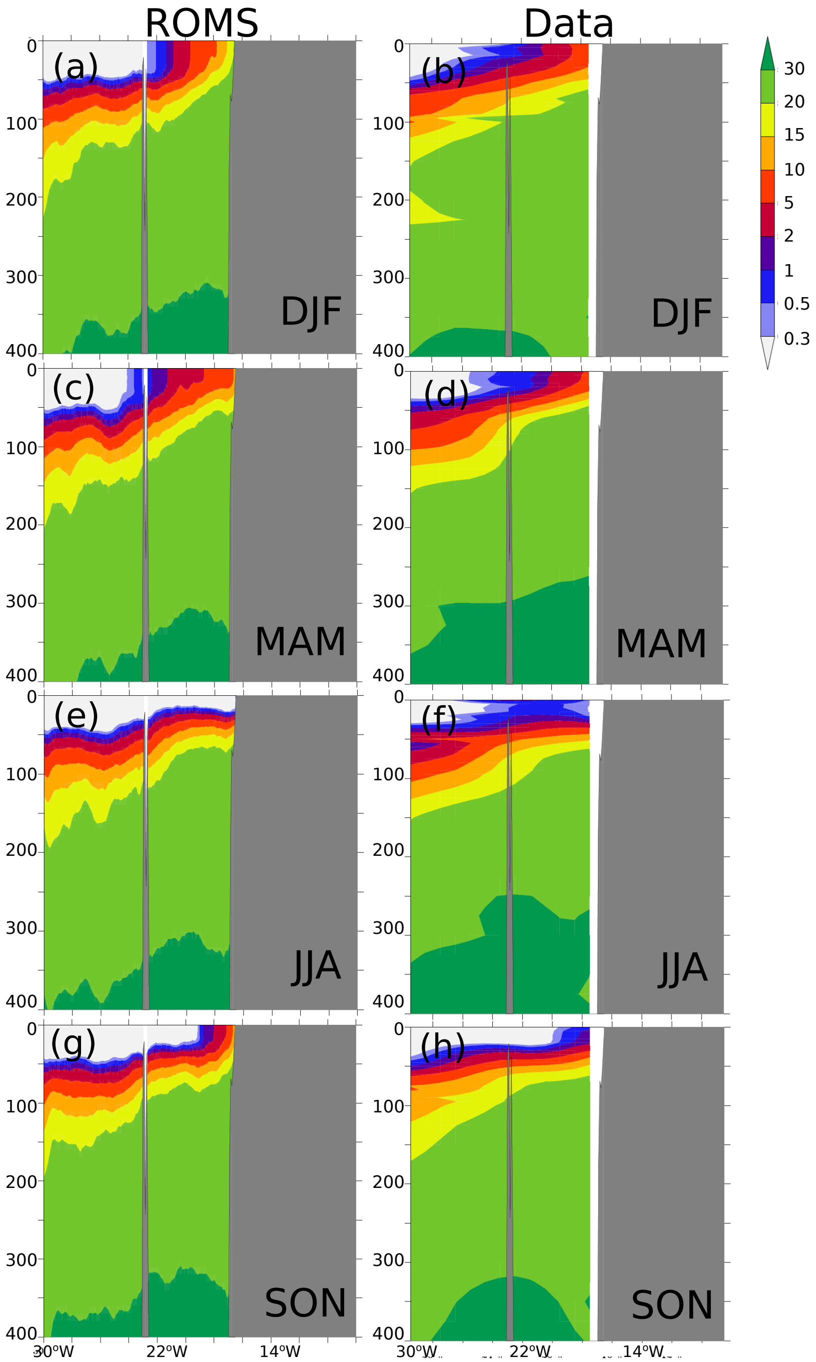

Figure S12. Comparison of vertical cross section of nitrate across a transect at 16°N in the top 400m between the model and World Ocean Atlas observations.

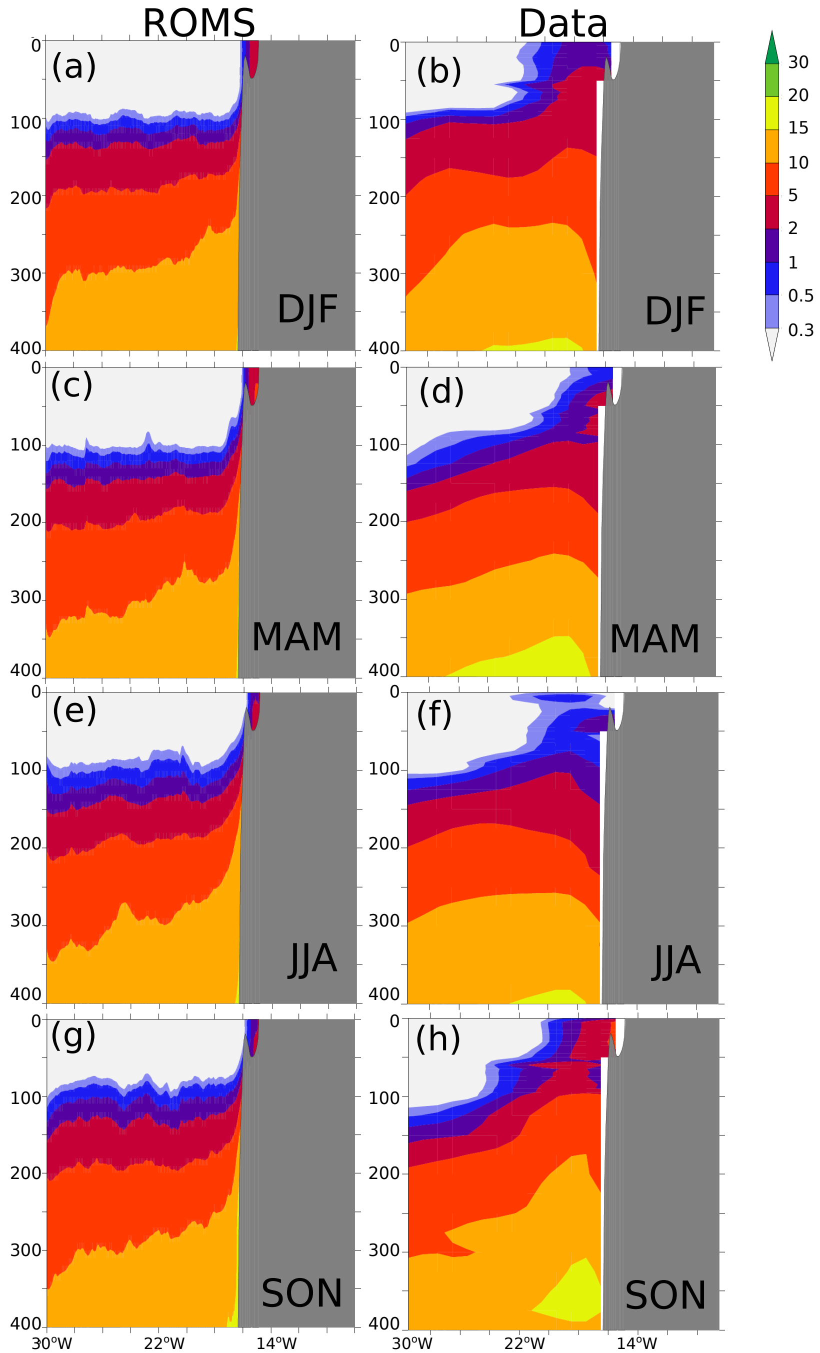

Figure S13. Comparison of vertical cross section of nitrate across a transect at 25°N in the top 400m between the model and World Ocean Atlas observations.

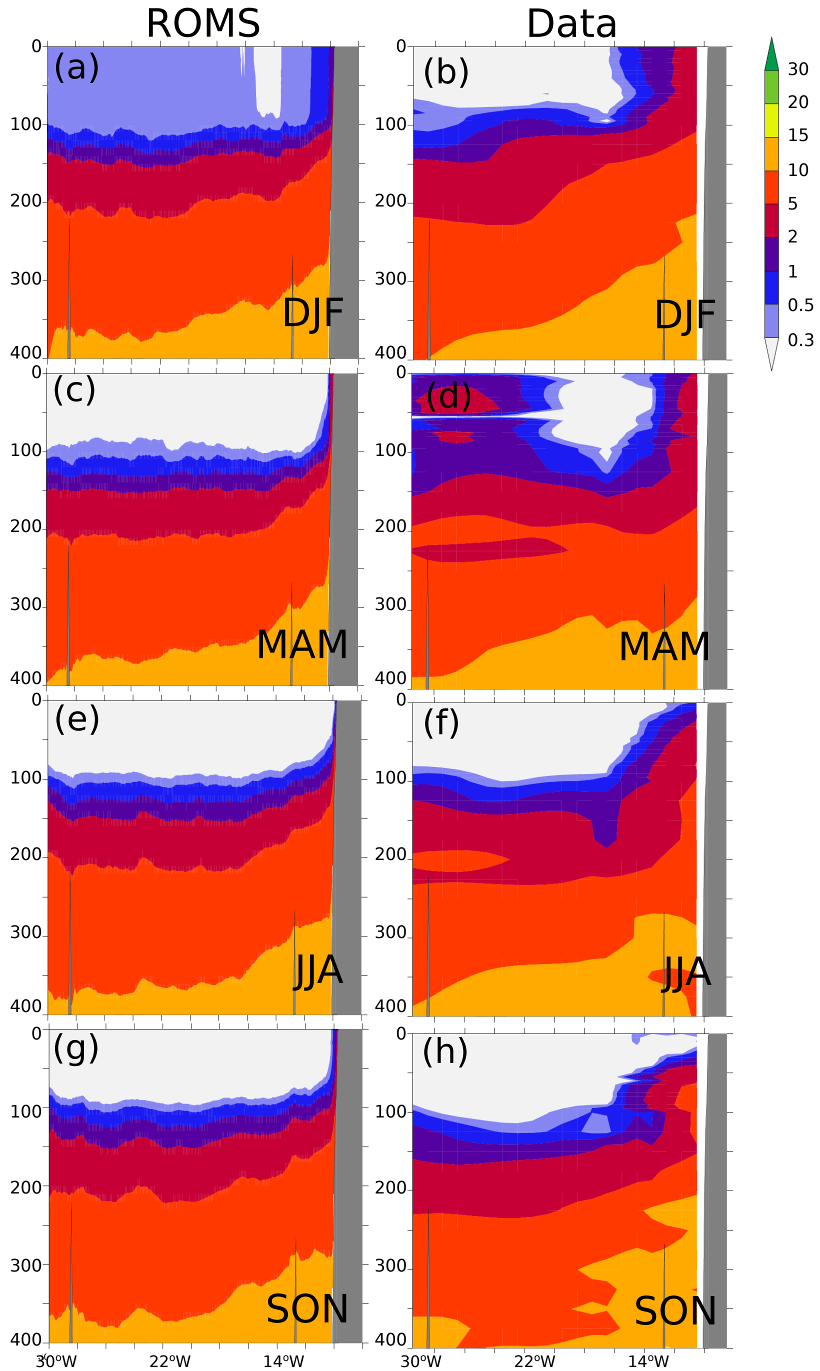

Figure S14. Comparison of vertical cross section of nitrate across a transect at 30°N in the top 400m between the model and World Ocean Atlas observations.

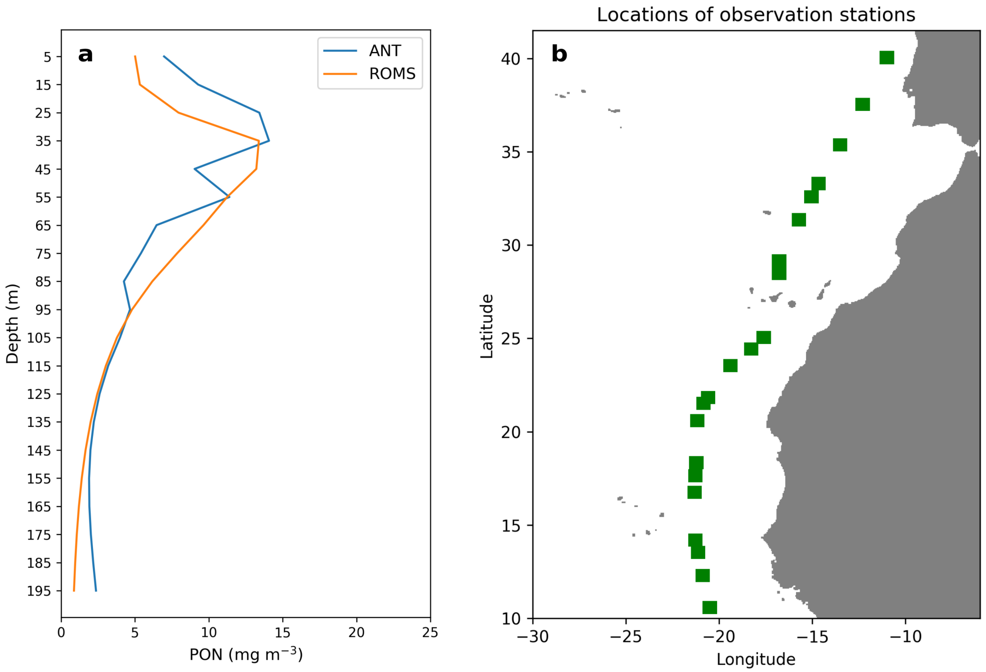

Figure S15. (a) Comparison of vertical profile of POC at several in situ observation stations part of the ANT campaign and the POC simulated in our model. (b) The locations of the observation stations we consider. For an observation at a given depth, the values across all stations are averaged. In our model, POC values at each depth is averaged for all locations co-located with the observation stations. All POC values are binned to 10 m depth ranges.

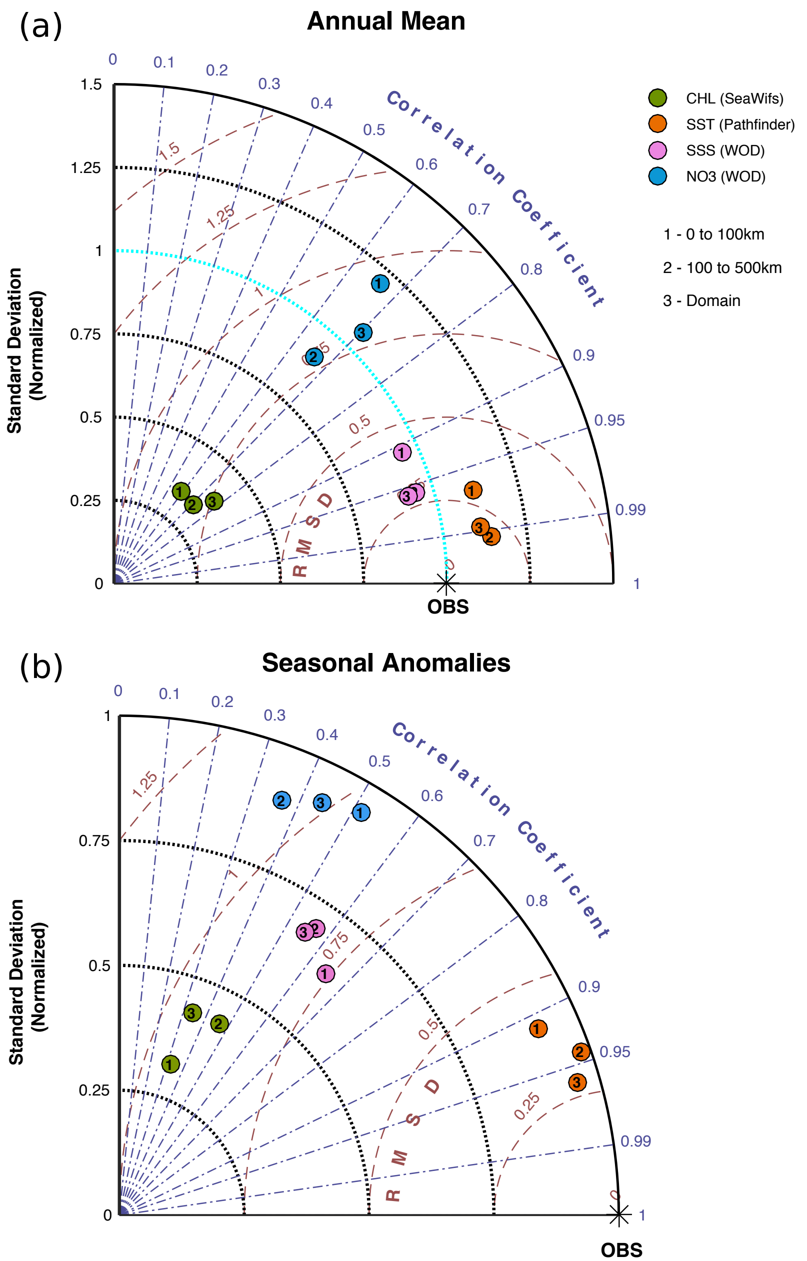

Figure S16. Taylor diagrams describing statistical comparisons of modeled and observed (a) annual mean and (b) seasonal anomaly estimates of sea surface temperature (orange), salinity (pink), NO_3^- (blue) and chlorophyll-a (green) in the 0-100 km nearshore region (data points labeled "1"), the 100-500 km offshore region (data points labeled "2") and across the entire model domain (data points labeled "3"). The reference point of the Taylor diagram corresponds to SeaWiFS observations for chlorophyll, AVHRR data for sea surface temperature, world ocean database (WOD) 2013 for surface salinity and nitrate.

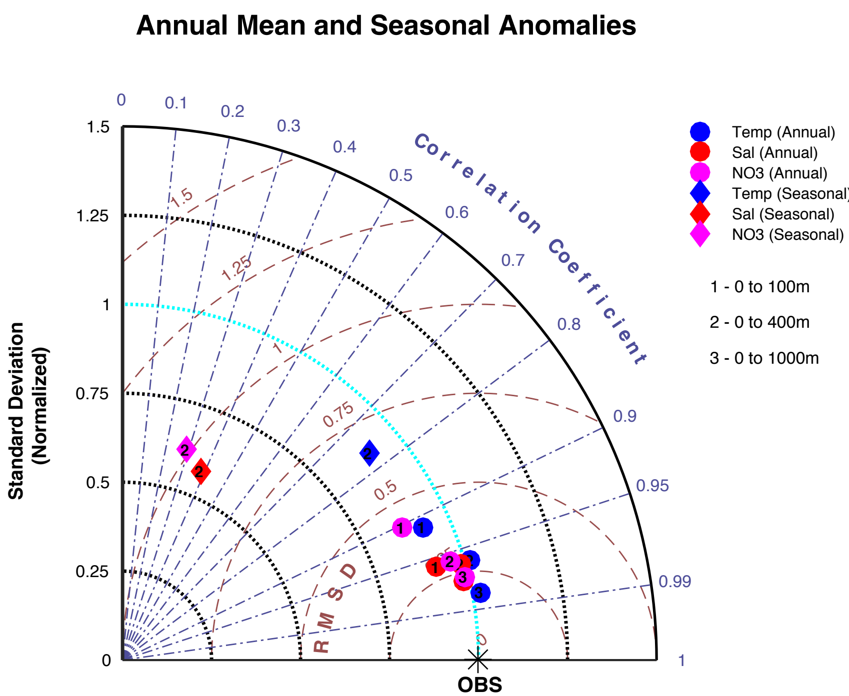

Figure S17. Taylor diagrams displaying statistical comparisons of modeled and observed annual mean (circular) and seasonal anomaly (diamond) estimates of temperature (blue), salinity (red) and NO_3^- (pink) in the top 100 m (data points labeled "1"), top 400 m (data points labeled "2") and top 1000 m (data points labeled "3"). The reference point of the Taylor diagram corresponds to AVHRR data for temperature, world ocean database (WOD) 2013 for salinity and nitrate.

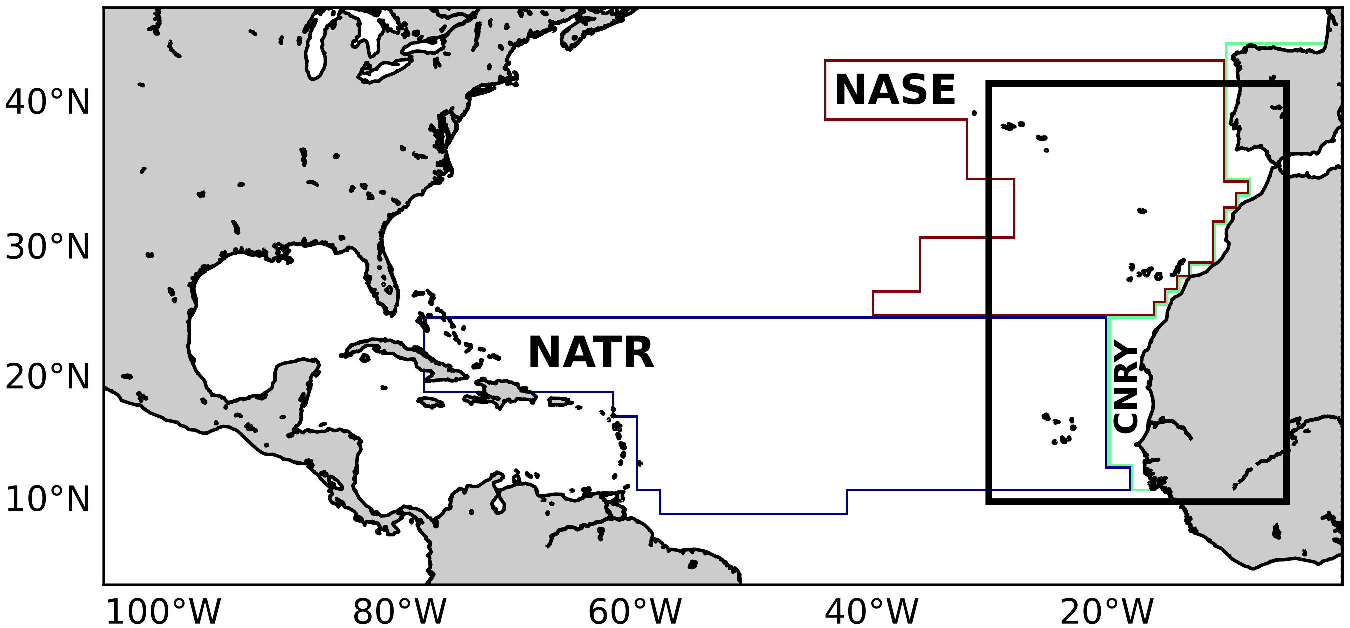

Figure S18. Geographical limits of the CNRY (green), NATR (blue) and NASE (red) Longhurst provinces. The black box shows the regional limit of our ROMS model domain. The total surface areas of the NATR and NASE are 8.2 and 4.4 million km^2, respectively.

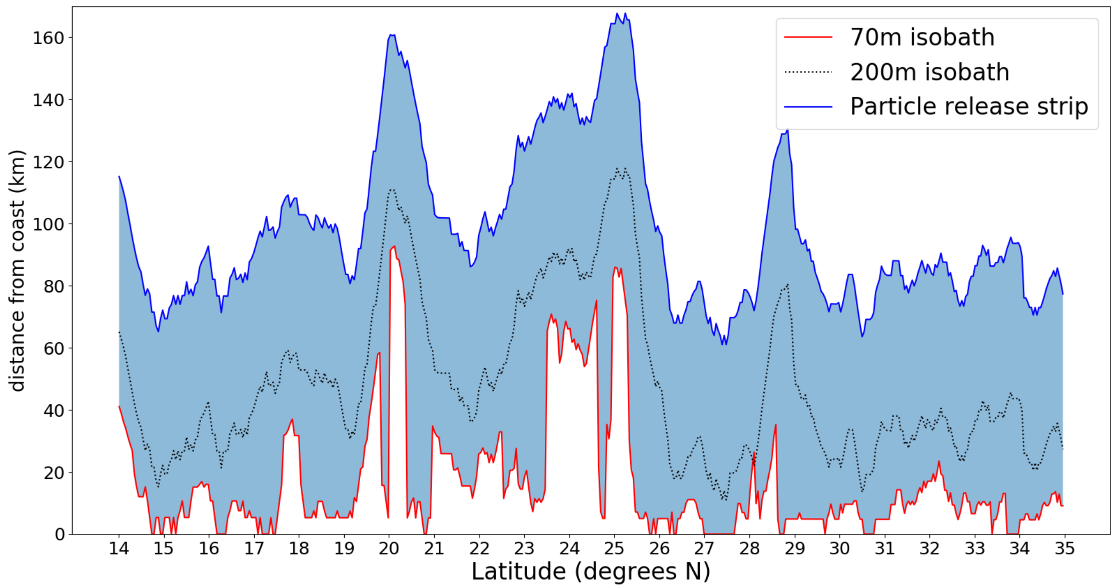

Figure S19. The distance from coast of the 70m isobath, 200m isobath and the particle release strip. The particle release strip uniformly lies 50km west of the 200m isobath. In our tracking experiment, particles that upwell between the 70m isobath and the particle release strip (in the blue shaded area) are considered.

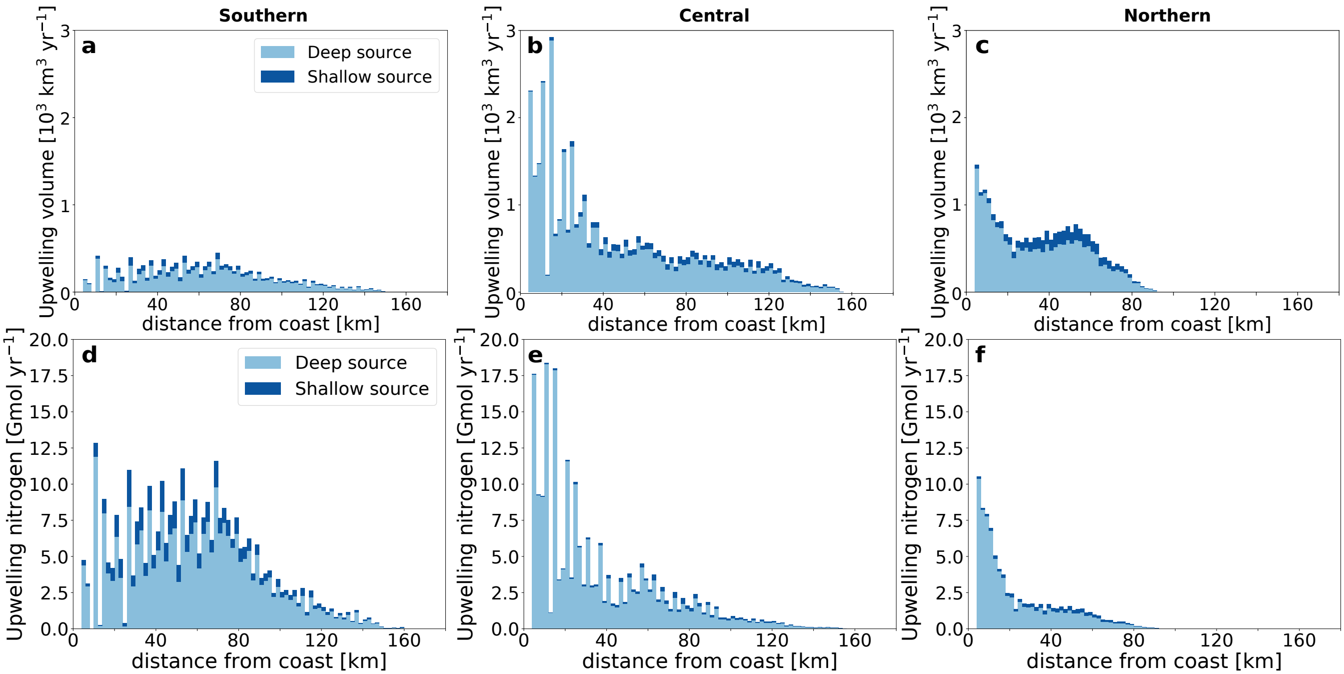

Figure S20. Zonal distribution of upwelling volume (a-c) and nitrogen content (d-f) at different distances from the coast for the three subregions of the CanCS. While the maximum of the upwelling in the Southern subregion occurs offshore at round 70 km distance from the shore with weak cross-shore differences, the central subregion has a clear maximum in upwelling in the first 20 km from the shore. The amount of upwelling then declines sharply with increasing offshore distance. The northern subregion has a first upwelling volume maximum right at the coast and a secondary maximum around 50 km. Beyond 80 km, there is hardly any upwelling. Generally, parcels that upwell further from the coast carry a nitrogen flux that is disproportionately lower than their corresponding associated water volume.

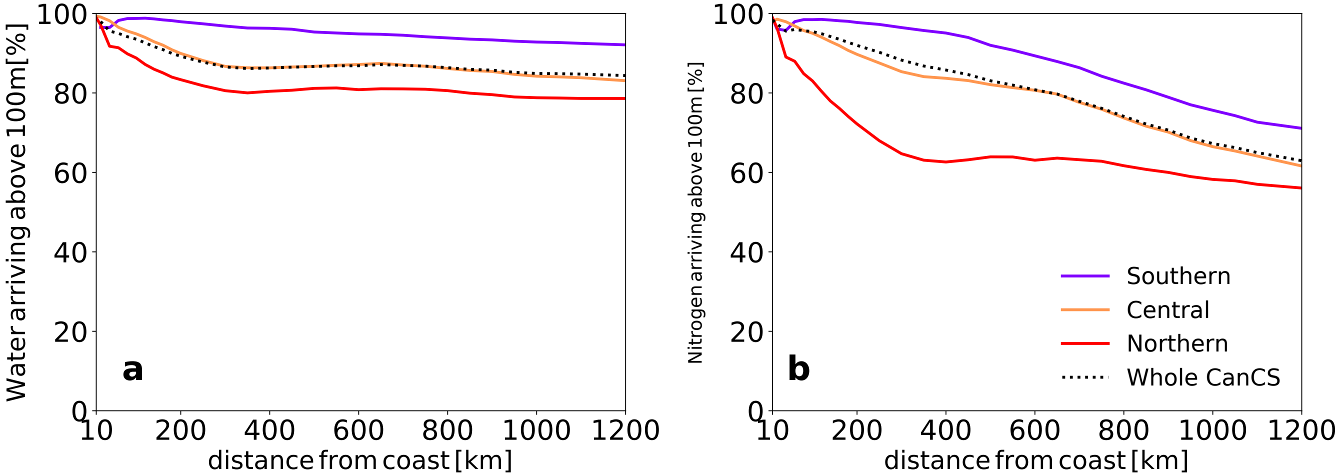

Figure S21. Fraction (in %) of upwelled (a) water and (b) nitrogen that remains above 100 m at their first arrival to each offshore distance in the three subregions as well as the entire CanCS region in our experiment.

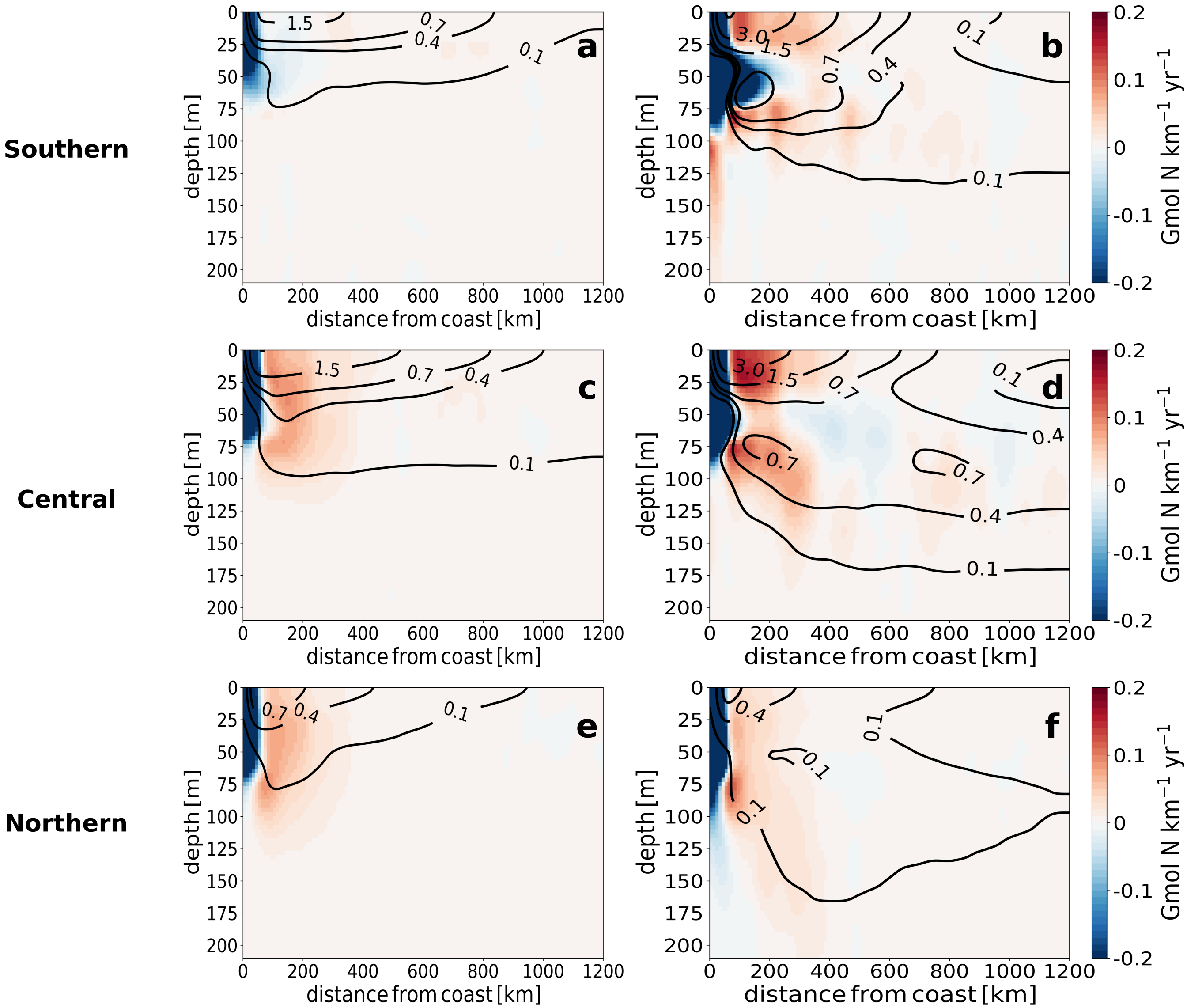

Figure S22. Meridionally integrated net downward and offshore transports of organic (left) and inorganic (right) nitrogen in the upper 200 m as a function of the distance to the coast in the three subregions in our experiment. Color shading shows the downward transport (in Gmol N km^{-1} yr^{-1}) while contours correspond to the offshore transport (in Gmol N m^{-1} yr^{-1}).

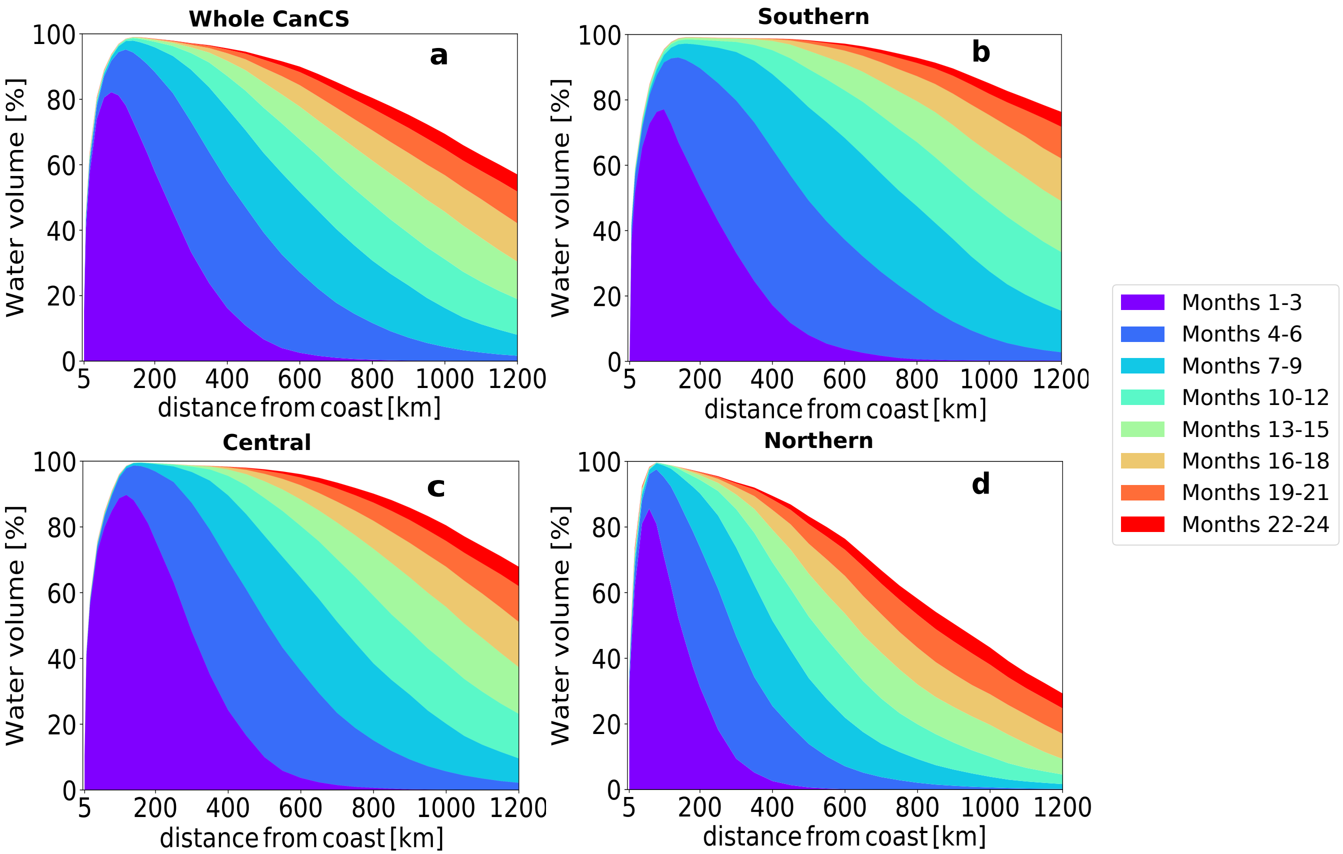

Figure S23. Upwelling water volume that first reaches each distance in each 3-month period of the total 2-year trajectories for the three subregions and the entire CanCS region in our experiment.

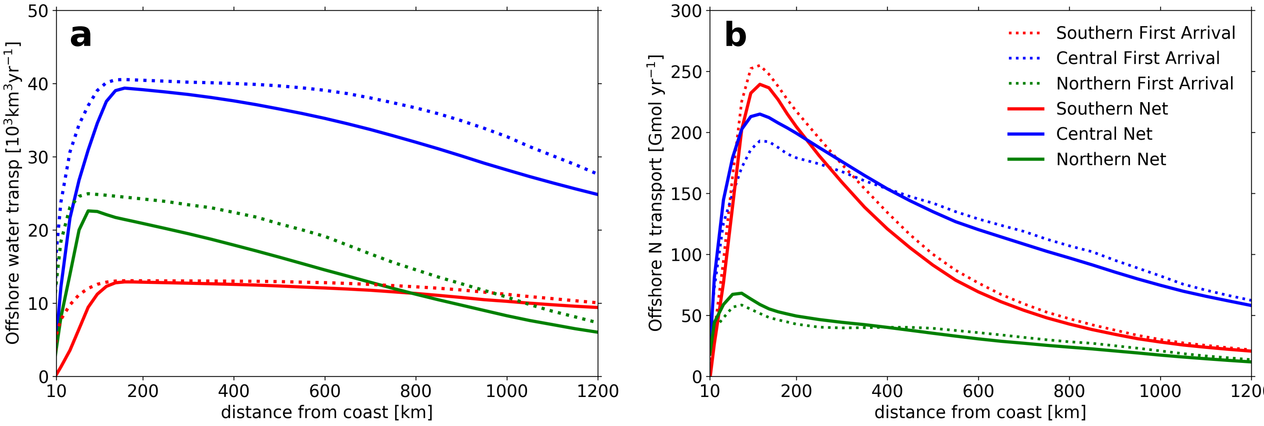

Figure S24. The annual average (a) water and (b) nitrogen carried to each distance by upwelled particles at their first arrival (dashed lines) and as net transport (solid lines) in each subregion. First arrival volume to a given distance is equal to total transport (net transport + net recirculation), thus exceeding net transport, for water while it may be higher or lower than net transport for nitrogen.

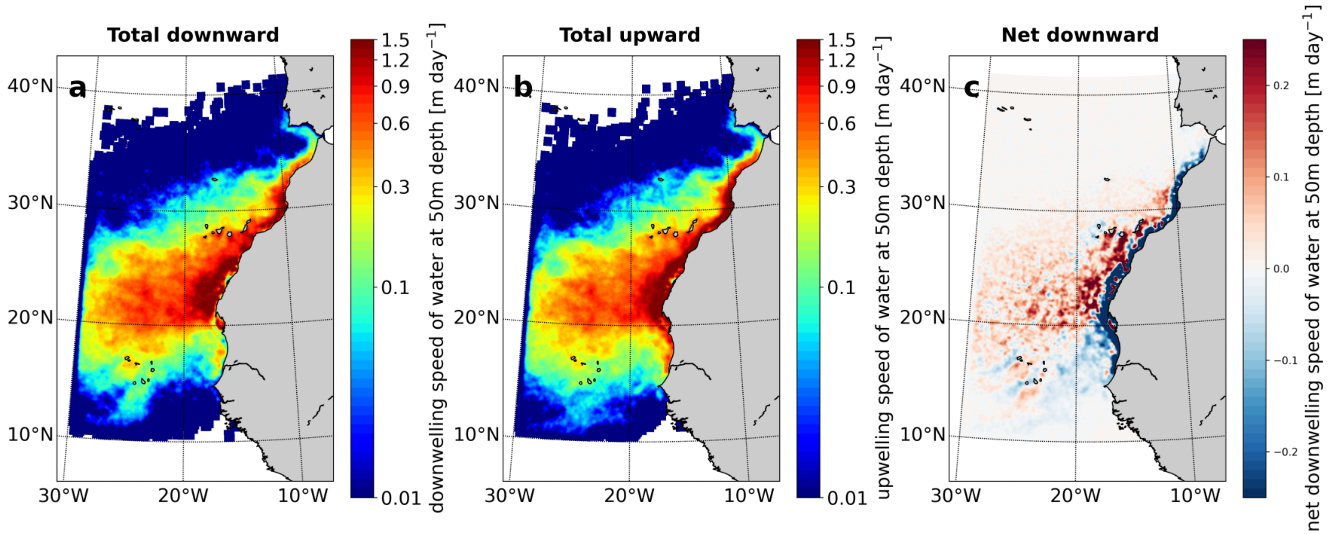

Figure S25. Horizontal distribution of vertical transport of water at 50m depth in the entire domain. (a) Total downward transport speed. (b) Total upward transport speed. (c) Net downward transport speed. In (a, b), we added the associated volumes of all particles that crossed 50 m downward and upward, respectively, throughout the 2 year particle trajectory experiment. In (c), the difference between (a) and (b) is taken.

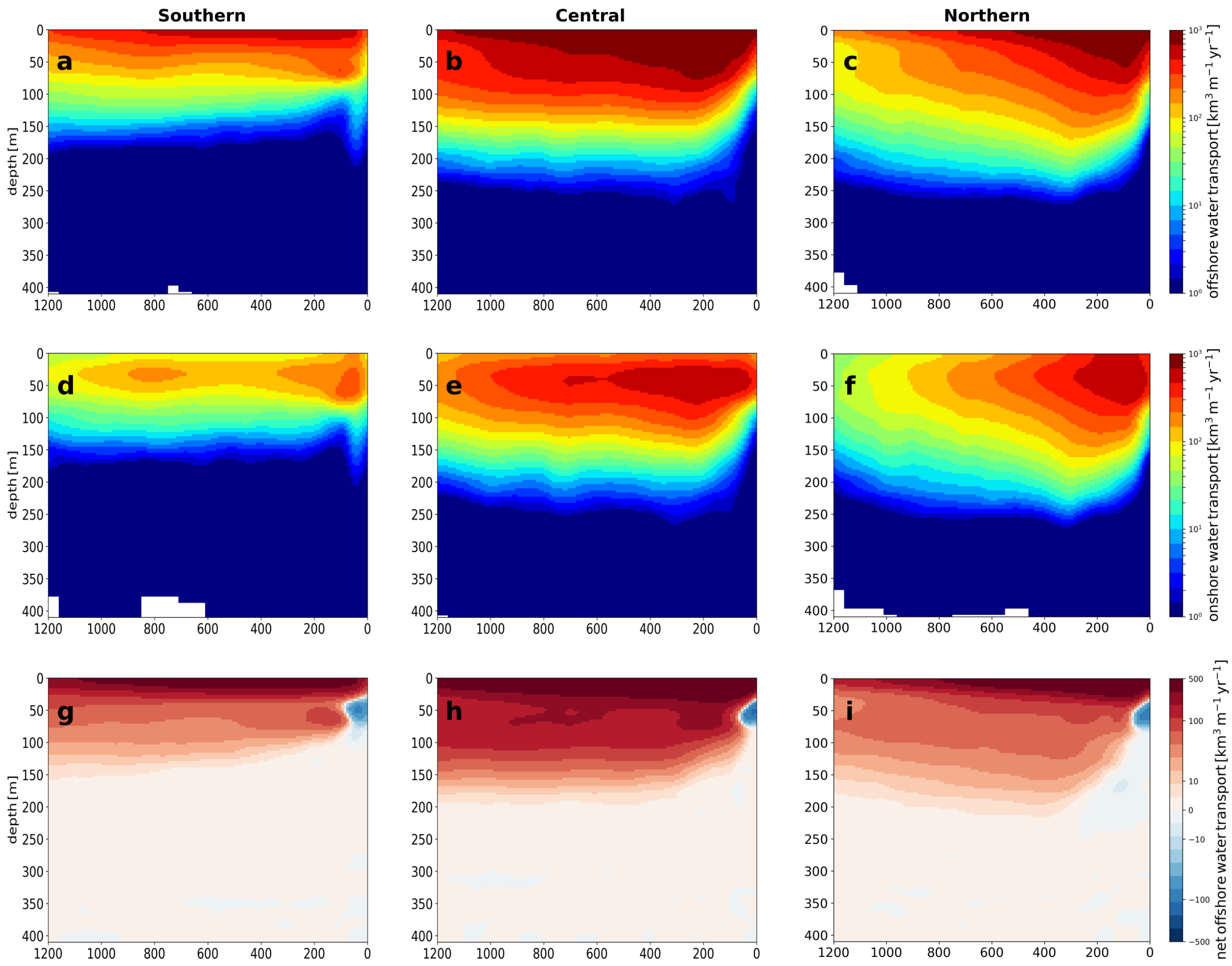

Figure S26. Meridionally integrated offshore transport of water. All values are in km^3 of water per a meter of depth per year. The columns (left to right) show the southern, central and northern subregions while the rows (top to bottom) show total offshore transport, total onshore transport and net offshore transport, all in logarithmic scales.

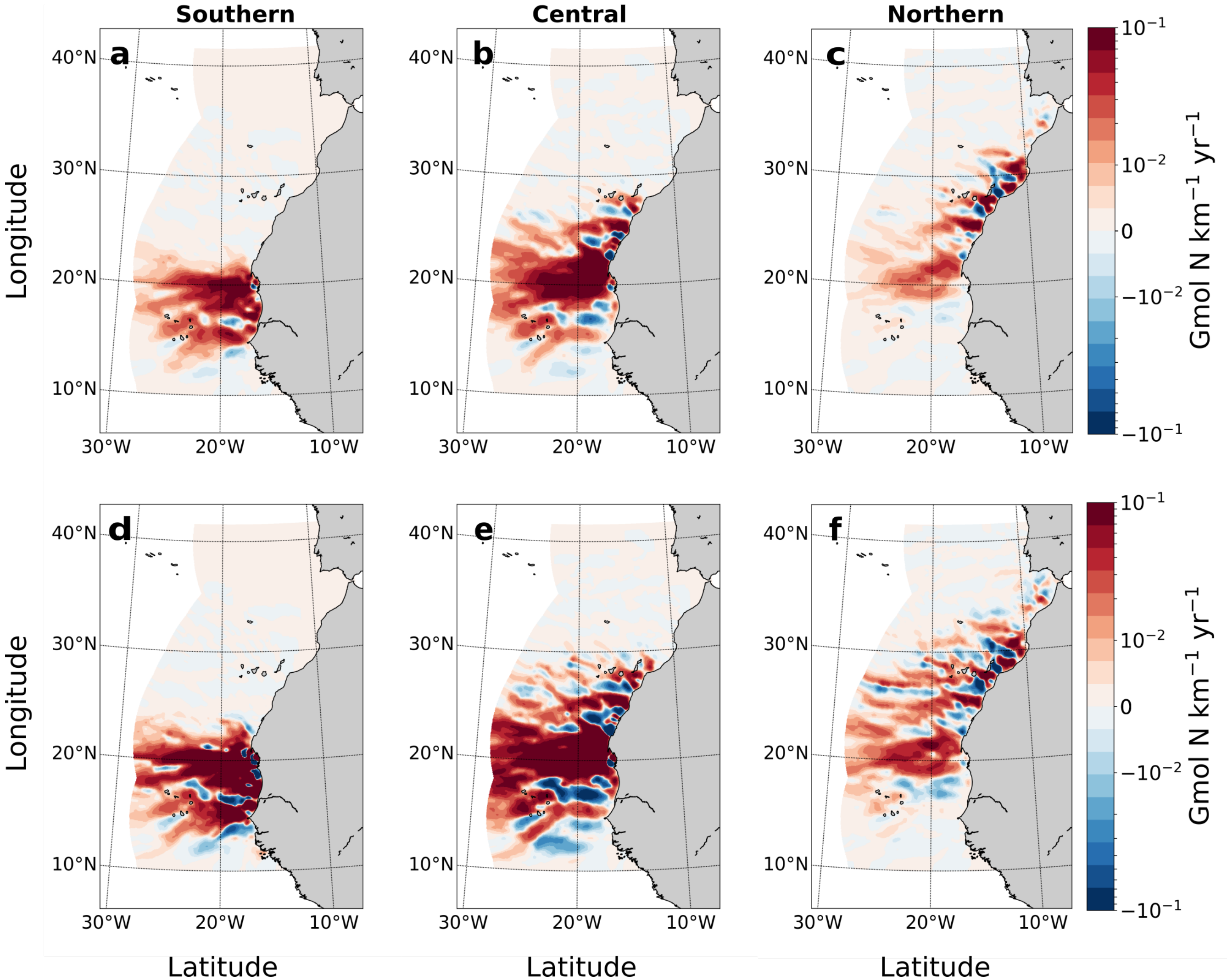

Figure S27. Horizontal distribution of vertically integrated offshore transport of organic (top) and inorganic (bottom) nitrogen in the three subregions.

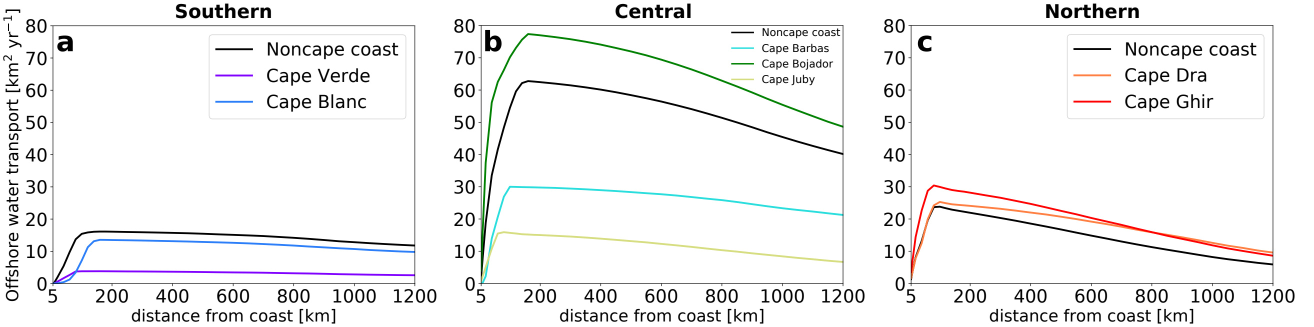

Figure S28. Net offshore transport of water by particles upwelling locally in each cape or non-cape coast in (a) the southern, (b) the central and (c) the northern CanCS. Note that the transport is normalized by coastal length (divided by the length of the coast at the respective cape or non-cape).

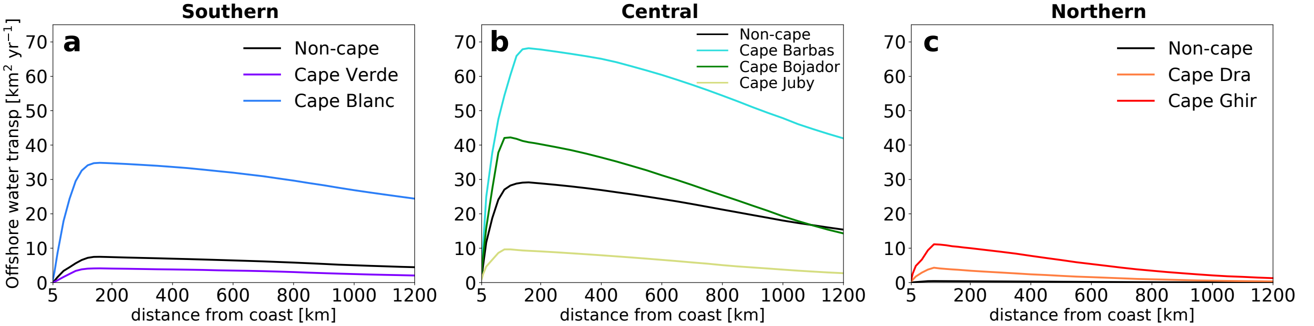

Figure S29. Net offshore transport of water by particles that leave the coastal upwelling region at each cape or non-cape area but upwell non-locally in (a) the southern, (b) the central and (c) the northern CanCS. Note that the transport is normalized by coastal length (divided by the length of the coast at the respective cape/non-cape).

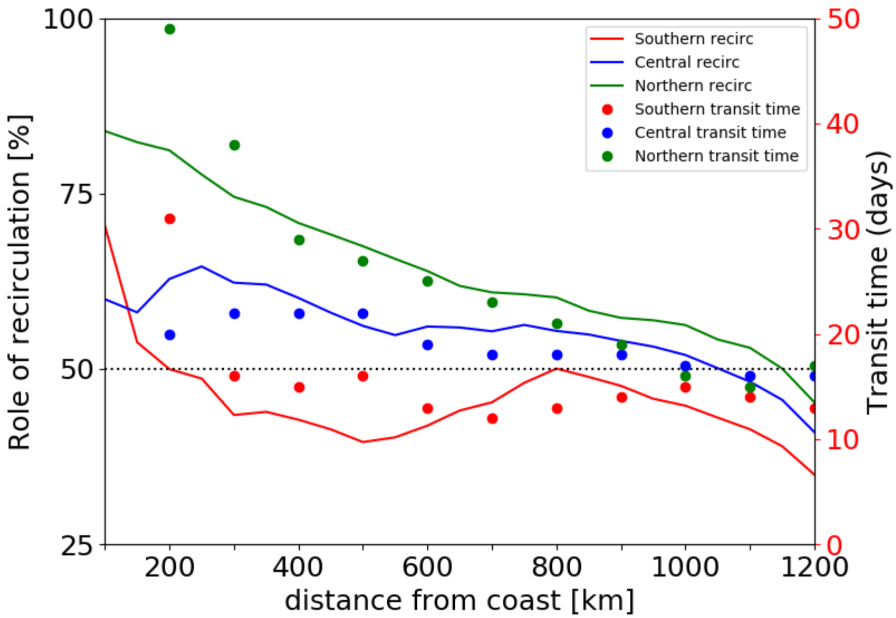

Figure S30. Total water recirculation (indirect transport + net recirculation) (filled circles) and median transit times (solid lines) at different offshore distances for the southern (red), the central (blue) and the northern (green) CanCS. Median transit times at each offshore distance is the median time particles take to cross the 100 km that precedes the given distance.

	200km	400km	600km	800km	1000km	1200km
Southern	84	146	208	268	332	385
Central	59	131	214	298	369	430
Northern	126	252	361	434	473	517
Whole CanCS	83	169	254	329	391	443

Table S1. The median residence time (days) of particles between upwelling and reaching each distance for the three subregions as well as the entire CanCS region in our experiment.

	Latitude range (°N)	Coast length (km)
C. Verde	14.5-15.5	192
C. Blanc	20-21	195
C. Barbas	22-22.75	112
C. Bojador	25-26.5	210
C. Juby	27.5-28.5	238
C. Dra	28.5-29.5	169
C. Ghir	30-31	139

Table S2. Latitudinal range of major capes and their coastal length (in km).

	Our results	Lovecchio et al. (2017)
100 km	12.3	18.8
500 km	6.9	8.2
1,000 km	2.5	4.6

Table S3. Comparison of net offshore export of organic carbon (in Tg C yr^{-1}) by upwelling particles at different distances from the coast between our experiment and estimates based on Lovecchio et al. (2017).

Table S4. Comparison of POC offshore transport estimates in the CanCS region from previous studies and from the present study. Note that our model-based estimates correspond to annual mean climatologies whereas observation-based estimates listed in the table are based on data collected from different individual campaigns that took place either in August or September. All values are given in kg C s^{-1} with a C:N ratio of 6.625 assumed in our model.

Previous study	Latitude	Longitude (offshore dist.)	Depth	Time	Transport estimate	This study
Alonso-González et al. (2009)	20°N-29.2°N	20.35°W	0m-73m	7-29 Sep, 2003	161.3	109.8
	-	26°W	0m-135m	-	212.7	40.3
García-Muñoz et al. (2004)	27.6°N-27.85°N	13.7°W	0m-100m	13-26 Aug, 1999	18.8	10.6
García-Muñoz et al. (2005)	30.8°N-32.4°N	11.25°W	0m-100m	26 Sep-2 Oct, 1997	11.2	5.6
Santana-Falcon et al. (2016)	30.2°N-31.2°N	10.6°W	0m-100m	26-27 Aug, 2009	20.9	3.4
Lovecchio et al. (2017)	17°N-24.5°N	100km	0m-100m	Annual mean	404	273.3
	-	500 km	-	-	207	176.8
	-	1000 km	-	-	70	61.1
	24.5°N-32°N	100km	-	-	198	93.2
	-	500 km	-	-	34	16.1
	-	1000 km	-	-	11	3.2

Table S5. Estimates of annual mean offshore transport of nitrogen (in Gmol N yr^{-1}) in the California and Benguela upwelling systems from previous studies. Organic nitrogen is considered in both particulate organic nitrogen (PON) and dissolved organic nitrogen (DON) forms.

Prvious study	Latitude	Longitude (offshore dist.)	Depth	Form	Offshore transport
Gutknecht et al., 2013	18°S-35°S	10°E	0m-50m	PON	340 ± 144.5
	-	-	-	DON	93.5 ± 42.5
	-	-	-	NO_3 + NO_2+ NH_4	289 ± 144.5
Frischknecht et al., 2018	34°N-41°N	100km	0m-100m	PON + DON	160
	-	-	-	NO_3 + NH_4	187
	32°N-41°N	500km	-	PON + DON	90
	-	-	-	NO_3 + NH_4	78